Chapter 8
Numerical Basics of Bioimpedance Measurements

Alexander Danilov, Sergey Rudnev, and Yuri Vassilevski

8.1 Introduction

Bioimpedance measurements estimate passive electric properties of biological tissues in response to application of a low-level alternating electric current (see Grimnes and Martinsen 2014). The measurements form a basis for a number of safe, noninvasive, portable, and relatively low-cost techniques of health monitoring, such as impedance cardiography (ICG) (Cybulski 2011), impedance plethysmography (IPG) (Jindal et al. 2016), electrical impedance tomography (EIT) (Holder 2005), and bioimpedance analysis of body composition and spectroscopy (BIA, BIS) (Jaffrin and Morel 2008; Bera 2014).

In BIA and BIS, simple representation of the human body as a homogeneous isotropic cylindrical conductor is used to assess body composition and body fluids (Jaffrin and Morel 2008; Brantlov et al. 2016). A few contact electrodes (usually four or eight) are utilized to obtain whole body, segmental body, or local body characteristics from measured transfer impedance at single or multiple current frequencies. Similarly, a small number of electrodes (typically, four band or eight spot ones) are used in measurements of the transfer impedances for the assessment

A. Danilov (✉) · Y. Vassilevski
Institute of Numerical Mathematics, Russian Academy of Sciences, Moscow, Russia

Moscow Institute of Physics and Technology, Moscow, Russia

Sechenov University, Moscow, Russia

S. Rudnev
Institute of Numerical Mathematics, Russian Academy of Sciences, Moscow, Russia

Lomonosov Moscow State University, Moscow, Russia

Federal Research Institute for Health Organization and Informatics, Moscow, Russia

of central hemodynamics in ICG (Cybulski 2011; Bera 2014). The same applies for the evaluation of vascular function in IPG (Jindal et al. 2016).

The human body is highly inhomogeneous anisotropic structure. The most promising way of substantiation and further development of the above methods, as well as accurate data interpretation, is accounting this inhomogeneity by using high-resolution mathematical models of the human body. Such models are used to identify the source of bioimpedance signal and proper electrode placement in ICG (Kauppinen et al. 1998; Belalcazar and Patterson 2004; Patterson 2010) and to find optimal electrode configuration and frequency range for the detection of lung edema in BIS (Beckmann et al. 2007; Ulbrich et al. 2013).

In a sense, EIT is an extension of BIA and BIS to a larger number of electrodes which are needed for reconstruction of conductivity distribution in the body from measured transfer impedance data (Holder 2005). Since EIT is an imaging technique, it exploits various software tools generating anatomically correct discrete models of the body that improve the quality of reconstructed images (Bayford et al. 2001; Adler et al. 2015). The discrete model of the body constituents allows to generate a computational mesh which is the basis for application of a finite element method (FEM). The latter is appealing in bioengineering simulations since, in contrast to finite difference methods, it can use very general meshes which discretize fine anatomical structures. An alternative and competitive discretization method, the finite volume method, has weaker theoretical basis and may be more sensitive to mesh properties.

In this chapter, we present essential elements and the workflow of the FEM-based computational technology (Danilov et al. 2017) in bioimpedance modeling (Danilov et al. 2012, 2013; Vassilevski et al. 2012). The cornerstone of the technology is an anatomically correct 3D model of the human body from the Visible Human Project (VHP) (Ackerman 2003). The outline of the chapter is as follows. In Sect. 8.2, we formulate the mathematical model of electrical fields generated during bioimpedance measurements. The 3D image segmentation, adaptive mesh generation process, and finite element discretization are considered, and the convergence of the proposed numerical method is analyzed in Sect. 8.3. The traditional approach to identification of regions of high measurement sensitivity is presented in Sect. 8.4. In Sect. 8.5, we introduce an online numerical simulator of bioimpedance measurements which models the conventional 4-electrode and 10-electrode placement schemes (Danilov et al. 2017). A summary of the proposed numerical technology, its advantages, limitations, and future prospects are discussed in Sect. 8.6. Section 8.7 collects conclusive remarks.

8.2 Mathematical Model

The mathematical model of bioimpedance measurements is based on the following stationary boundary value problem (see, e.g., Danilov et al. 2012; Grimnes and Martinsen 2014):

$$\text{div}(\mathbf{C}\nabla U) = 0 \quad \text{in} \quad \Omega, \tag{8.1}$$

$$(\mathbf{J}, \mathbf{n}) = I_0/S_\pm \quad \text{on} \quad \Gamma_\pm, \tag{8.2}$$

$$(\mathbf{J}, \mathbf{n}) = 0 \quad \text{on} \quad \partial\Omega \backslash \Gamma_\pm, \tag{8.3}$$

$$U(x_0, y_0, z_0) = 0, \tag{8.4}$$

$$\mathbf{J} = \mathbf{C}\nabla U. \tag{8.5}$$

In these equations Ω is the computational domain, $\partial\Omega$ is its boundary, $\Gamma_\pm$ are the electrode contact surfaces, $\mathbf{n}$ is the outward unit normal vector, U is the electric potential, $\mathbf{C}$ is the conductivity tensor allowing to describe anisotropic materials, $\mathbf{J}$ is the current density, I_0 is the electric current, and $S_\pm$ are the areas of the electrode contacts. Equation (8.1) determines the distribution of electric field in the domain with heterogeneous conductivity $\mathbf{C}$. Equation (8.2) sets the constant current density on the electrode contact surfaces. Equation (8.3) defines the no-flow condition on the boundary. Uniqueness of the solution is guaranteed by Eq. (8.4), where (x_0, y_0, z_0) is a given point inside the domain Ω.

In order to analyze the response of materials to alternating electric fields, it is convenient to replace the conductivity with a complex tensor called the *admittivity*. Admittivity is the sum of a real component called the conductivity and an imaginary component called the susceptivity. Typical values of some materials and tissues admittivity are presented in Table 8.1 (Vassilevski et al. 2012).

The conventional measurement technique involves two pairs of electrodes attached to the skin. The first pair of *current carrying* (CC) electrodes is used for injecting electrical current into the body. The second pair of *pick-up* (PU) electrodes is used for measuring the electric potential difference. This difference divided by the value of injected current is called the *transfer impedance*.

Table 8.1 Admittivity of some tissues and materials at different frequencies, Sm/m (Vassilevski et al. 2012)

Material	Admittivity @ 5 kHz		Admittivity @ 50 kHz	
	Conductivity	Susceptivity	Conductivity	Susceptivity
Skin	0.0015	0.002	0.03	0.05
Heart	0.13665	0.0356	0.19543	0.047215
Lungs	0.23484	0.0183	0.26197	0.02372
Abdominal tissues	0.10–0.12	0.0045–0.0055	0.11–0.13	0.007–0.009
Contact electrode layer	0.9	0.01	0.9	0.01
External electrode layer	10	0	10	0

8.3 Computational Technology

The approximate solution of (8.1)–(8.5) is provided by the finite element method with P_1 (continuous piecewise linear) basis functions on unstructured tetrahedral meshes. We assume that each computational element has a constant admittivity coefficient related to one of the human tissues.

We can rewrite Eq. (8.1) with complex values as a system of two equations with real values:

$$\text{div}(\mathbf{C_R}\nabla U_R) - \text{div}(\mathbf{C_I}\nabla U_I) = 0 \quad \text{in} \quad \Omega,$$
$$\text{div}(\mathbf{C_R}\nabla U_I) + \text{div}(\mathbf{C_I}\nabla U_R) = 0 \quad \text{in} \quad \Omega, \tag{8.6}$$

where $\mathbf{C} = \mathbf{C_R} + i\mathbf{C_I}$ and $U = U_R + iU_I$.

The FEM discretization is based on the weak formulation of (8.2)–(8.6). One seeks U_R, U_I from the Sobolev space $W_2^1(\Omega)$, that satisfy the identities

$$\int_{\Omega} \mathbf{C_R}\nabla U_R \nabla V \, d\Omega - \int_{\Omega} \mathbf{C_I}\nabla U_I \nabla V \, d\Omega - \int_{\Gamma_{\pm}} VI_0/S_{\pm} \, d\Gamma_{\pm} = 0,$$
$$\int_{\Omega} \mathbf{C_R}\nabla U_I \nabla V \, d\Omega + \int_{\Omega} \mathbf{C_I}\nabla U_R \nabla V \, d\Omega = 0 \tag{8.7}$$

for arbitrary function V from $W_2^1(\Omega)$. Let a conformal tetrahedral mesh be given in Ω. We construct the subspace $W_{2,h}^1(\Omega)$ of the Sobolev space $W_2^1(\Omega)$ composed of functions which are continuous in Ω, linear in each mesh tetrahedron and vanish at the point (x_0, y_0, z_0). Substituting $W_2^1(\Omega)$ by $W_{2,h}^1(\Omega)$ in the weak formulation (8.7) we arrive at a system of linear equations

$$A_R \mathbf{U}_R - A_I \mathbf{U}_I = \mathbf{F}_R,$$
$$A_I \mathbf{U}_R + A_R \mathbf{U}_I = \mathbf{F}_I, \tag{8.8}$$

where $\mathbf{U}_R$ and $\mathbf{U}_I$ are vectors of coefficients in the expansion of the approximate FEM-solutions U_R^h, U_I^h with the FEM basis functions.

In order to substantiate the numerical scheme, we consider a simple geometrical model of the human torso (Vassilevski et al. 2012) (Fig. 8.1) and a series of unstructured tetrahedral meshes with variable element size. For each mesh we compute the numerical solution and compare it with the numerical solution obtained on the finest mesh by using L_2-norm to evaluate the difference between the numerical solutions.

We consider the series of hierarchical meshes. The initial coarse mesh contains 9359 tetrahedra. Starting from this mesh, we decompose each tetrahedron into 8 smaller tetrahedra by splitting each face into four triangles by the middle points on the edges. We call this operation a uniform refinement of the mesh. Now we can apply the uniform refinement to the new mesh, and so on. At each step the

Fig. 8.1 Simplified geometrical model of the human torso used for the convergence study
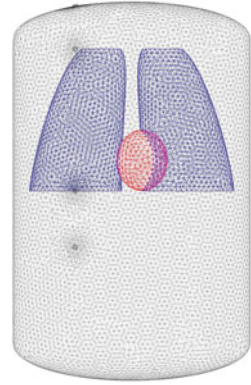
Table 8.2 The results of the convergence study on hierarchical meshes

N_V	N_T	Memory (Mb)	N_{it}	Time (s)	L_2-norm
2032	9359	7.16	13	0.02	1.24E−03
14,221	74,872	37.3	23	0.18	9.31E−04
106,509	598,976	299.1	58	3.70	5.07E−04
824,777	4,791,808	2437.5	127	68.55	1.53E−04
6,492,497	38,334,464	20,015.3	353	2634.15	–

element size of the mesh is decreased in two times. The finest mesh in the series of five meshes has more than 38 millions tetrahedra and requires nearly 20 GB of the memory for computation. We used GMRES based iterative linear solver with the second-order ILU preconditioner (Kaporin 1998). All necessary routines were taken from the open source library Ani3D (Lipnikov and Vassilevski 2007).

The results of the convergence study on the series of hierarchical meshes are presented in Table 8.2. The first two columns show the number of vertices N_V and the number of tetrahedra N_T. The next three columns show the memory usage, the number of linear solver iterations N_{it} needed for the 10^{12}-fold reduction of an initial residual, and the overall time usage, respectively. The last column contains the relative L_2-norm that reduces asymptotically with roughly the second order convergence. If the meshes are not nested hierarchically, the error estimate requires extra interpolation of the finite element solution onto the finest grid. Application of this interpolation reduces the convergence order to one on non-nested meshes.

The numerical scheme verified on the simplified discrete model of the torso can be applied to a high-resolution human body geometrical model. The model was constructed in two steps. First, the geometrical model of the human torso was created for the VHP man data (Ackerman 2003). The data were clipped and downscaled to an array of 567×305×843 colored voxels with the resolution 1×1×1 mm. The initial segmented model of the VHP man torso was kindly provided by the Voxel-Man group (Höhne et al. 2000). This model has been produced primarily for visualization purposes, contained a significant amount of unclassified tissue and thus was not entirely suited for numerical purposes. Therefore, a further

Table 8.3 Admittivity of human body tissues at different electric current frequencies, Sm/m (Gabriel et al. 1996a,b; Vassilevski 2010)

Material	Admittivity @ 5 kHz		Admittivity @ 50 kHz	
	Conductivity	Susceptivity	Conductivity	Susceptivity
Blood vessels	0.50573	0.0031	0.50883	0.009496
Bones	0.051324	0.000532	0.052032	0.00122
Brain	0.088129	0.00881	0.102552	0.012525
Cartilage	0.17554	0.00169	0.17706	0.007679
Diaphragm	0.33669	0.0146	0.35182	0.028064
Esophagus	0.52811	0.00422	0.53369	0.009873
Eye	0.33369	0.005	0.33849	0.007302
Eye nerve	0.034567	0.0138	0.069315	0.026656
Fat	0.023589	0.000783	0.024246	0.000479
Gallbladder	0.90006	0.000064	0.90012	0.000317
Heart	0.13665	0.0356	0.19543	0.047215
Intestine	0.4393	0.011303	0.452783	0.023694
Kidney	0.12881	0.0193	0.15943	0.031776
Larynx	0.17554	0.00169	0.17706	0.007679
Liver	0.047666	0.0119	0.072042	0.029722
Lung	0.23484	0.0183	0.26197	0.02372
Muscle	0.33669	0.0146	0.35182	0.028064
Pancreas	0.52811	0.00435	0.53395	0.011185
Skin	0.0015	0.002	0.03	0.05
Spinal cord	0.034567	0.0138	0.069315	0.026656
Spleen	0.10829	0.00661	0.11789	0.015272
Stomach	0.52811	0.00422	0.53369	0.009873
Testis	0.37809	0.0049	0.385275	0.013202
Thyroid gland	0.52811	0.00435	0.53395	0.011185
Tongue	0.27812	0.00477	0.28422	0.015281
Trachea	0.30507	0.00984	0.32987	0.019219

processing of the segmented model was performed semi-automatically on the basis of ITK-SNAP segmentation software program (Yushkevich et al. 2006). At the final stage, we used several post-processing algorithms for filling remaining gaps between tissues and final segmented data smoothing (Serra 1984). Our segmented model of the human torso contains 26 labels describing tissues and major organs or their constituents (e.g., left/right kidney and lung, arteries/veins), with 22 admittivity properties presented in Table 8.3.

The segmented data are given on a very fine voxel grid; a coarser mesh with the same resolution of tissue interfaces should be used in computations. We tested several meshing techniques for the mesh generation of the segmented data. In our work we opted for the Delaunay triangulation algorithm from the CGAL-Mesh library (Rineau and Yvinec 2007). This algorithm enables defining a specific mesh size for each model material. In order to preserve geometrical features of the
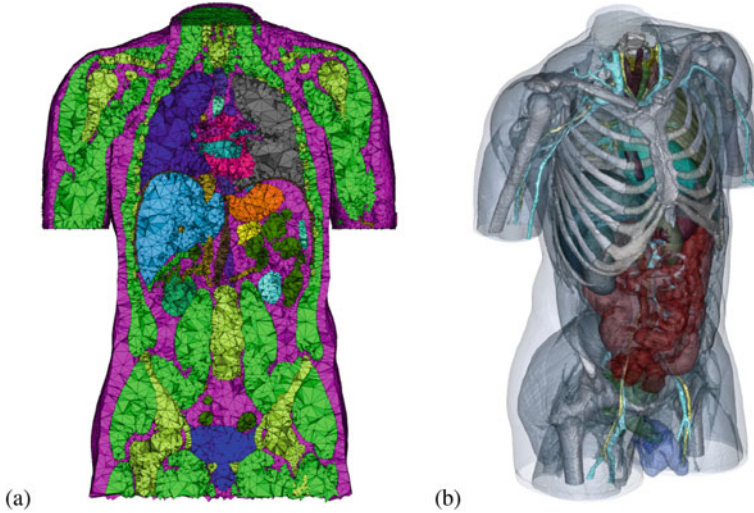
Fig. 8.2 Unstructured tetrahedral mesh (**a**) for geometrical model of the segmented image (**b**)

segmented model while keeping a feasible number of vertices, we assigned a smaller mesh size to blood vessels and a larger mesh size to fat and muscle tissues.

After the initial mesh generation, we applied mesh cosmetics from the Ani3D package (Lipnikov and Vassilevski 2007). This essential step reduces discretization errors and the matrix stiffness in the resulted systems of linear equations. The segmented model and the generated mesh containing 413,508 vertices and 2,315,329 tetrahedra are presented in Fig. 8.2. This mesh retains most anatomical features of the human torso.

In addition to the segmented torso model, we prepared a segmented model of the whole body. Missing parts were segmented using the ITK-SNAP software. The position of the arms was adapted manually by moving them away from the body (Danilov et al. 2013) as is the case with bioimpedance measurements. The final model is a 1100×333×1878 voxels array with the resolution 1×1×1 mm segmented with 30 labels associated with organs, their constituents and other tissues, altogether 26 materials with admittivites presented in Table 8.3. We used the same approach to construct the computational mesh for the whole body model based on the VHP data. The related segmented model and generated mesh containing 479,198 vertices and 2,725,980 tetrahedra are shown in Fig. 8.3.

After mesh generation for the torso and the whole body, we added a skin layer and multilayered electrodes to the surface of the constructed mesh. The original boundary triangulation was used to create a prismatic mesh on the surface, and then each prism was split into three tetrahedra resulting in a conformal tetrahedral mesh.

A series of computational meshes were generated in accordance with different positions of electrodes. Along with the conventional tetrapolar wrist-to-ankle measurement configuration (4-electrode scheme), a 10-electrode segmental BIA
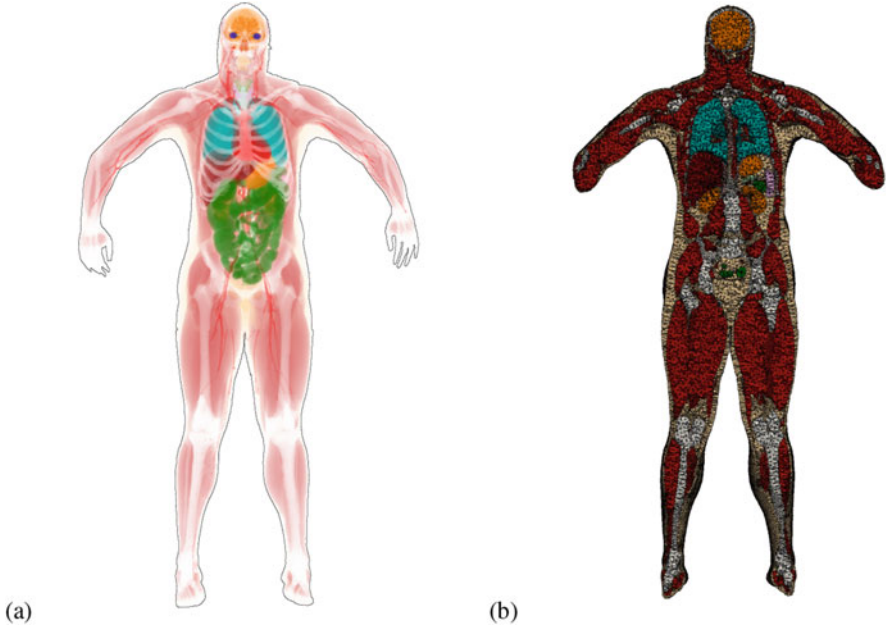
Fig. 8.3 Segmented whole body model of the VHP man with stretched arms (**a**) and a cut of the generated mesh by the frontal plane (**b**)

measurements scheme was considered with the placement of current and potential electrodes at a mutual distance of 5 cm on the back surfaces of the wrists and ankles, and also on the forehead (Fig. 8.4). Accordingly, five pairs of thin bilayer square objects 23×23 mm in size as electrodes were added on the forehead and distal parts of arms and legs of the segmented model.

8.4 Sensitivity Analysis

Sensitivity analysis is used to visualize the regions contributing most to the measured transfer impedance for the tetrapolar scheme measurements.

In order to perform the sensitivity analysis, we introduce the reciprocal lead field $\mathbf{J}'_{\text{reci}}$ which is equal to density vector field generated by a unit current excitation using the two PU electrodes. Field $\mathbf{J}'_{\text{reci}}$ is computed from (8.1)–(8.5), with electrode surfaces $\Gamma_\pm$ corresponding to PU electrodes and $I_0 = 1$ (Geselowitz 1971; Grimnes and Martinsen 2014) (Fig. 8.5b).
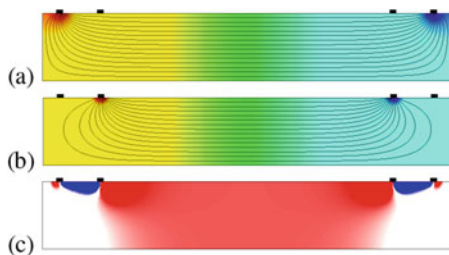
The lead field may be used for sensitivity distribution analysis of the PU electrodes for CC electrodes. We will use the following two equations: the general transfer signal equation

$$u = \int_\Omega \rho \, \mathbf{J}_{\text{cc}} \cdot \mathbf{J}'_{\text{reci}} \, \mathrm{d}x, \tag{8.9}$$
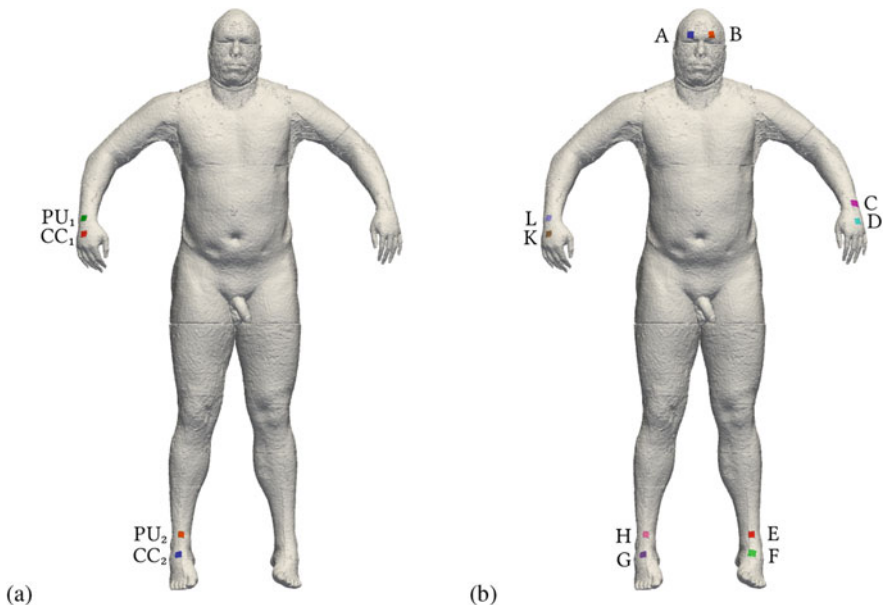
Fig. 8.4 Electrode positions for the conventional tetrapolar wrist-to-ankle measurement configuration (**a**) and the 10-electrode segmental BIA scheme (**b**)

Fig. 8.5 Sensitivity analysis of the tetrapolar scheme on a homogeneous cylinder, cross section through the electrode plane: (**a**) electric potential and current lines for CC pair; (**b**) electric potential and current lines for PU pair; (**c**) sensitivity field: red, positive; blue, negative; white, nearly zero sensitivity

and the general transfer impedance equation:

$$Z_t = \int_\Omega \rho \, \mathbf{J}'_{cc} \cdot \mathbf{J}'_{reci} \, dx. \tag{8.10}$$

In these equations, u is the measured signal between PU electrodes, ρ is the resistivity, $\mathbf{J}_{cc}$ is computed from (8.1)–(8.5) with electrode surfaces $\Gamma_\pm$ corresponding to the current carrying electrodes (Fig. 8.5a), Z_t is the transfer impedance, and $\mathbf{J}'_{cc} = \mathbf{J}_{cc}/I_0$.

The sensitivity analysis is based on the distribution of the sensitivity field, which is computed as

$$S = \mathbf{J}'_{\text{cc}} \cdot \mathbf{J}'_{\text{reci}}. \tag{8.11}$$

Sensitivity multiplied by resistivity is called *volume impedance density*.

Using this notation, we have the following relations:

$$Z_t = \int_\Omega \rho\, S\, dx, \quad \Delta Z_t = \int_\Omega \Delta\rho\, S\, dx. \tag{8.12}$$

The last formula is applicable only to relatively small changes of ρ and moderate variations in S.

For sensitivity analysis purposes, we shall split the domain Ω in three parts according to the value of the sensitivity field (Fig. 8.5c):

$$\Omega^- = \{\mathbf{x}|S(\mathbf{x}) < 0\}, \quad \Omega^+ = \{\mathbf{x}|S(\mathbf{x}) > 0\}, \quad \Omega^0 = \{\mathbf{x}|S(\mathbf{x}) = 0\}. \tag{8.13}$$

We can introduce the positive and negative components of the transfer impedance:

$$Z_t^+ = \int_{\Omega^+} \rho\, S\, dx, \quad Z_t^- = \int_{\Omega^-} \rho\, S\, dx, \quad Z_t = Z_t^+ + Z_t^-. \tag{8.14}$$

In addition, for a specific threshold value $t \in [0, 100]$, we shall define W_t^- as a subdomain of Ω^- and W_t^+ as a subdomain of Ω^+ with the following restrictions:

$$\inf_{\mathbf{x}\in\Omega\backslash W_t^-} \rho(\mathbf{x})S(\mathbf{x}) \geq \sup_{\mathbf{x}\in W_t^-} \rho(\mathbf{x})S(\mathbf{x}), \quad \int_{W_t^-} \rho\, S\, dx = \frac{t}{100} Z_t^-, \tag{8.15}$$

$$\sup_{\mathbf{x}\in\Omega\backslash W_t^+} \rho(\mathbf{x})S(\mathbf{x}) \leq \inf_{\mathbf{x}\in W_t^+} \rho(\mathbf{x})S(\mathbf{x}), \quad \int_{W_t^+} \rho\, S\, dx = \frac{t}{100} Z_t^+. \tag{8.16}$$

Thus, W_t^+ is the region of high volume impedance density, which have the transfer impedance contribution equal to t percents of the total transfer impedance. The same applies to W_t^-, which is the region of the most negative volume impedance density.

We shall also define subdomains V_t^+ and V_t^-:

$$\sup_{\mathbf{x}\in\Omega\backslash V_t^\pm} \pm S(\mathbf{x}) \leq \inf_{\mathbf{x}\in V_t^\pm} \pm S(\mathbf{x}), \quad \int_{V_t^\pm} S\, dx = \frac{t}{100} \int_{\Omega^\pm} S\, dx. \tag{8.17}$$

In our analysis we investigate the shape of the subdomains $W_t^\pm$ and $V_t^\pm$. These body regions represent the most sensitive parts of the human body for specified

measuring scenario. The shape of $W_t^\pm$ describes the part of the body in which one measures the positive and negative components $Z_t^\pm$ of the transfer impedance. The shape of $V_t^\pm$ represents the part which is the most sensitive to local changes of resistivity. This approach may be applied for validation of empirically designed electrode schemes.

If the media is homogeneous, the shape of the respective subdomains $V_t^\pm$ and $W_t^\pm$ will be the same. Figure 8.5 represents the sensitivity analysis of the tetrapolar scheme on a homogeneous cylinder. We can see two negative sensitivity areas between corresponding CC and PU electrodes, a positive sensitivity area between PU electrodes with a higher sensitivity near the PU electrodes, and two nearly zero sensitivity areas on both ends of the cylinder.

8.5 The Online Numerical Simulator

Within the above-described numerical modeling framework combining segmentation, mesh generation, FEM discretization, and post-processing techniques, the online numerical simulator of bioimpedance measurements was developed with publicly available user interface (Danilov et al. 2017). It is based on a JavaScript 3D library and WebGL technology. The segmented model of the VHP man with stretched arms (Fig. 8.3) is preloaded in the simulator. At present, the user can select either a 4-electrode or a 10-electrode measurement scheme (Fig. 8.4) with a predefined list of electrode pairs (Table 8.4). Optionally, the user may select manually the current carrying (CC) and pick-up (PU) electrode pairs.

Once the electrode pairs are selected, the server computes the respective solution of the boundary value problem (8.1)–(8.5), calculates the sensitivity field (8.11), and constructs the $V_t^\pm$ and $W_t^\pm$ regions. The user controls the threshold parameter t and examines the shape of $V_t^\pm$ or $W_t^\pm$.

Table 8.4 Electrode pairs for 10-electrode measurement scheme (rf. Fig. 8.4)

| Assessed body region	CC pair	PU pair
Left arm	D, B	C, E
Left leg	F, D	E, H
Right leg	G, F	H, L
Right arm	K, G	L, A
Head	B, K	A, C
Torso (parallel)	D, F	L, H
Torso (cross)	D, G	L, E
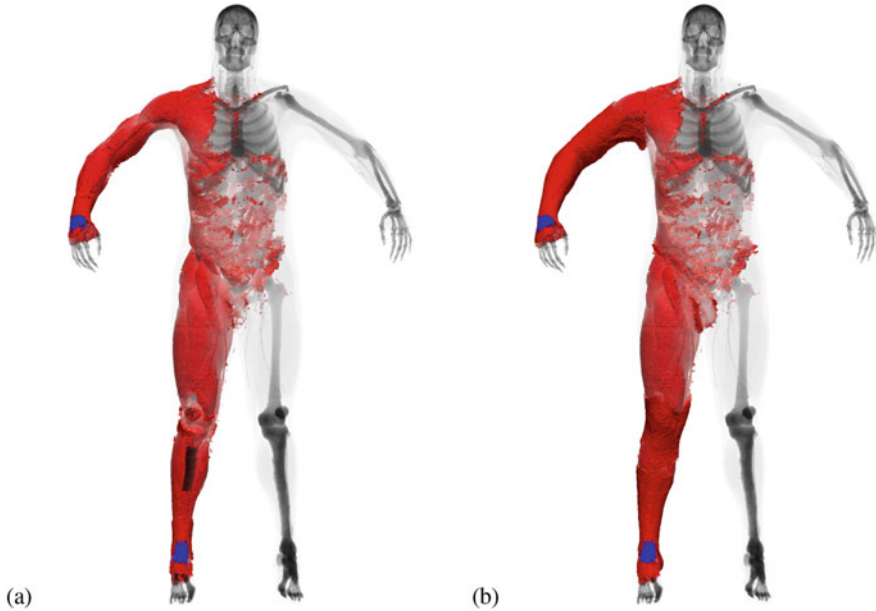
Fig. 8.6 Sensitivity analysis of the conventional 4-electrode scheme: (**a**) sensitivity distribution (red, V_{97}^+; blue, V_{97}^-); (**b**) volume impedance density distribution (red, W_{97}^+; blue, W_{97}^-)

High-resolution images of $V_{97}^{\pm}$ and $W_{97}^{\pm}$ regions overlaid on translucent body structure were constructed for the conventional 4-electrode (Fig. 8.6) and 10-electrode (Figs. 8.7, 8.8, 8.9) measurement schemes. Since the body structure is heterogeneous, the shapes of $V_t^{\pm}$ and $W_t^{\pm}$ are slightly different, though their general shape is the same. One can see the negative sensitivity area between the adjacent CC and PU electrodes in all the figures. The conventional wrist-to-ankle 4-electrode scheme demonstrates high sensitivity in the right arm, the right leg, and partially in the torso; the sensitivity in the head and the left arm and leg is nearly zero. It can be seen that the positive sensitivity areas in the 10-electrode scheme for various combinations of CC and PU electrode pairs listed in Table 8.4 well correspond to the respective names of body regions. The noticeable negative sensitivity areas in the 10-electrode scheme actually have minor impact on the transfer impedance, since the absolute values of Z_t^- are much smaller than Z_t^+ (Table 8.5).

8.6 Discussion

Computerized models of real human anatomy and digital human phantoms are extensively used in various areas of biomedicine such as radiography, nuclear medicine and radiation protection (Caon 2004; Xu 2014), as well as for educational
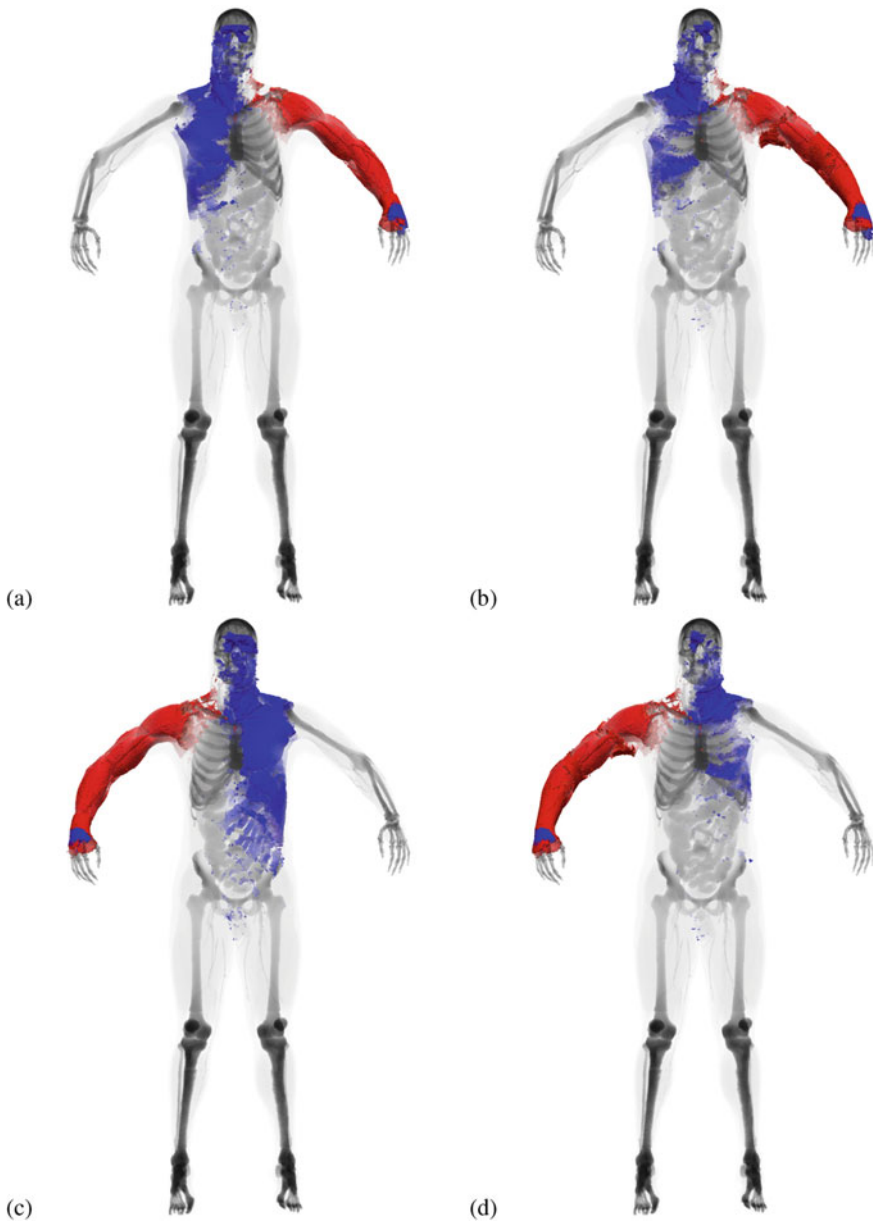
Fig. 8.7 Sensitivity analysis of the left (**a,b**) and right (**c,d**) arms using the 10-electrode scheme: (**a,c**) sensitivity distribution (red—V_{97}^+, blue—V_{97}^-); (**b,d**) volume impedance density distribution (red—W_{97}^+, blue—W_{97}^-)
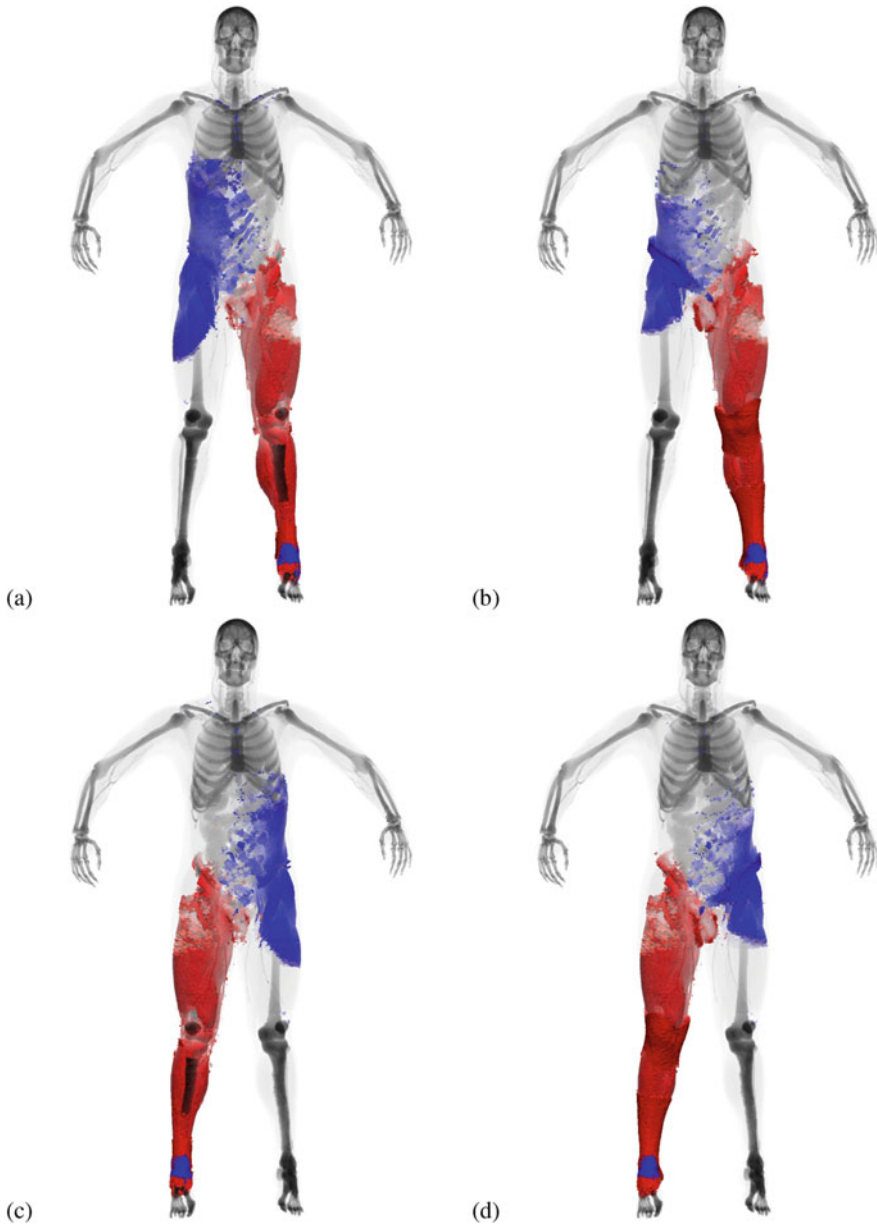
Fig. 8.8 Sensitivity analysis of the left (**a,b**) and right (**c,d**) legs using the 10-electrode scheme: (**a,c**) sensitivity distribution (red, V_{97}^{+}; blue, V_{97}^{-}); (**b,d**) volume impedance density distribution (red, W_{97}^{+}; blue, W_{97}^{-})
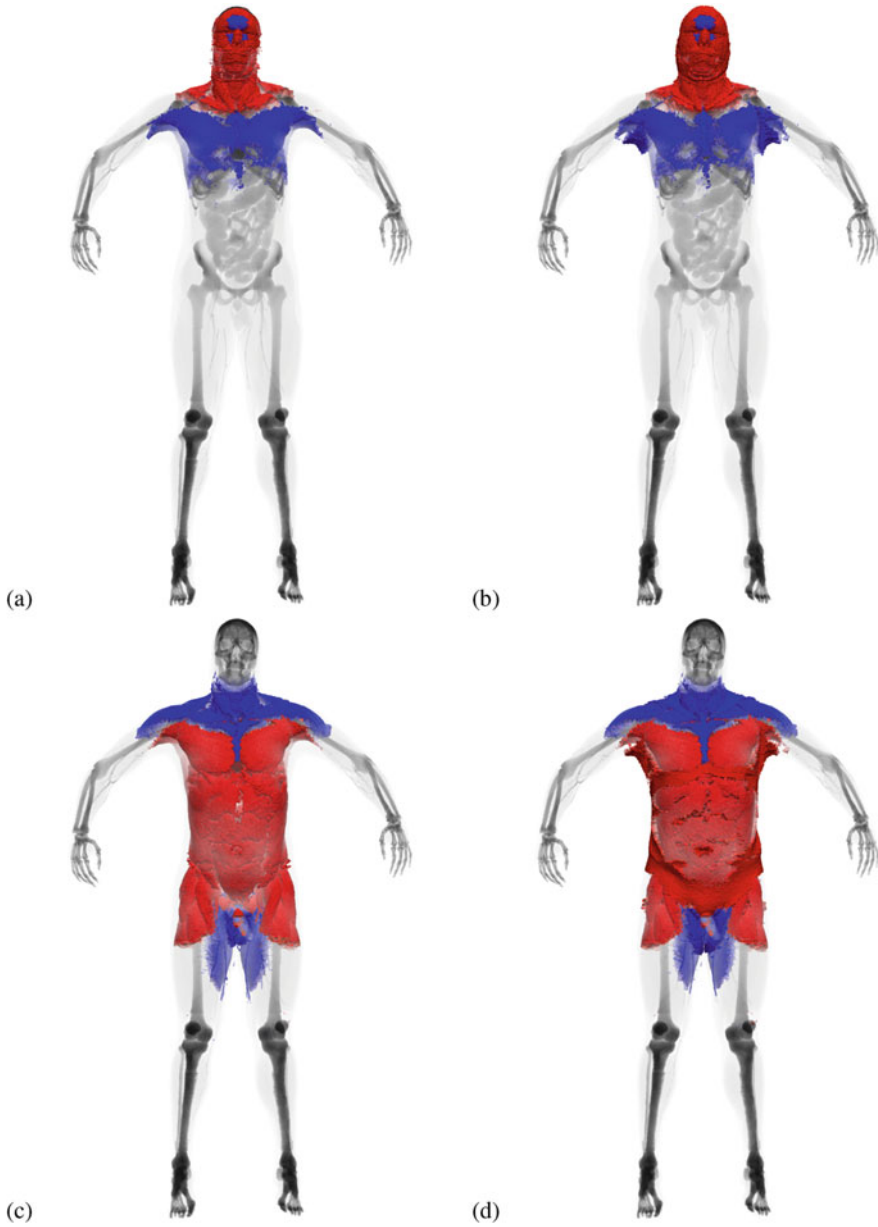
Fig. 8.9 Sensitivity analysis of the head (**a,b**) and torso (**c,d**) using the 10-electrode scheme: (**a,c**) sensitivity distribution (red, V_{97}^{+}; blue, V_{97}^{-}); (**b,d**) volume impedance density distribution (red, W_{97}^{+}; blue, W_{97}^{-})

Table 8.5 Contribution of positive and negative sensitivity areas to the transfer impedance

Measurement scheme	Z_t^+	Z_t^-	Z_t
Wrist-to-ankle	1004.84	−58.0518	946.79
Left arm	516.037	−35.8731	480.164
Right arm	558.69	−40.912	517.778
Left leg	413.024	−23.0604	389.963
Right leg	415.172	−23.418	391.754
Head	97.8496	−16.0922	81.7574
Torso (parallel)	38.1116	−5.62323	32.4884
Torso (cross)	38.1362	−5.7634	32.3728

and other purposes (Gosselin et al. 2014; Saltarelli et al. 2014). The same applies to bioimpedance methods of health monitoring, including impedance cardiography, electrical impedance tomography, and bioimpedance analysis of body composition and spectroscopy (Holder 2005; Jaffrin and Morel 2008; Cybulski 2011; Bera 2014; Jindal et al. 2016). High-resolution anatomically correct discrete models of the human body enable to study relative contribution of various organs and tissues to the bioimpedance signal, to find optimal electrode placement and electric current frequency range (Kauppinen et al. 1998; Belalcazar and Patterson 2004; Beckmann et al. 2007; Patterson 2010; Ulbrich et al. 2013; Orschulik et al. 2016). In electrical impedance tomography, such models are utilized to improve the quality of reconstructed images (Bayford et al. 2001; Adler et al. 2015).

In this chapter, the FEM-based computational technology and the online numerical simulator for high-resolution efficient modeling of bioimpedance measurements (Vassilevski et al. 2012; Danilov et al. 2012, 2013, 2017) are considered. The cornerstone of the technology is the anatomically correct 3D model of the VHP man (Ackerman 2003) and the finite element discretization of the stationary boundary value problem for the electric potential on tetrahedral meshes. FEM discretizations, in contrast to the conventional finite difference schemes on cubic meshes, account tissue anisotropy and provide more realistic description of electrical properties of the human body. The use of adaptive unstructured tetrahedral meshes makes our computational technology efficient: high-resolution models of the human body exploit significantly coarser meshes as compared to rectangular meshes thus reducing the computational cost. The limitations of the initial version of the online simulator are the use of the VHP man model only, fixed position of electrodes and, therefore, a limited number of measuring scenarios.

For other software and computational models used in the bioimpedance studies, we refer to Bayford et al. 2001, Pettersen and Høgetveit 2011, Adler et al. 2015, de Sitter et al. 2016. Validation of digital bioimpedance models can be performed by the MRI-based construction of an anatomically correct computational mesh of the measured subject and simulation of the bioimpedance measurements followed by the comparison with measured outcomes (Ulbrich et al. 2013). Bioimpedance applications utilizing finite element discretizations also include the development of new diagnostic tools (Ness et al. 2015), tissue engineering (Canali et al. 2015), and animal studies (Dowrick et al. 2016).

8.7 Conclusion

In this chapter, we presented essential elements and the workflow of the FEM-based high-resolution computational technology for modeling bioimpedance measurements. This technology is realized as the online numerical simulator with a user-friendly interface. The advantages of the technology are anatomically correct 3D model of the VHP man and the usage of FEM discretizations on the adaptive unstructured tetrahedral meshes. The technology allows to account tissue anisotropy and to adapt the mesh size and orientation of mesh faces for each organ/tissue geometry. Mesh adaptivity provides significant reduction of CPU time and computer memory requirements while saving the model accuracy. The simulator enables to calculate and visualize on a laptop sensitivity fields for the conventional tetrapolar and 10-electrode configurations at various measuring scenarios.

References

Ackerman, M. J. (2003). The National Library of Medicine's Visible Human Project. Accessed November 10, 2017. https://www.nlm.nih.gov/research/visible/

Adler, A., Lionheart, W. R. B., & Polydorides, N. (2015). EIDORS: electrical impedance tomography and diffuse optical tomography reconstruction software. Accessed November 10, 2017. http://eidors3d.sourceforge.net/

Bayford, R. H., Gibson, A., Tizzard, A., Tidswell, T., & Holder, D. S. (2001). Solving the forward problem in electrical impedance tomography for the human head using IDEAS (integrated design engineering analysis software), a finite element modelling tool. *Physiological Measurement, 22*(1), 55–64.

Beckmann, L., van Riesen, D., & Leonhardt, S. (2007). Optimal electrode placement and frequency range selection for the detection of lung water using bioimpedance spectroscopy. In *2007 29th Annual International Conference of the IEEE Engineering in Medicine and Biology Society* (pp. 2685–2688).

Belalcazar, A., & Patterson, R. P. (2004). Improved lung edema monitoring with coronary vein pacing leads: a simulation study. *Physiological Measurement, 25*(2), 475–487.

Bera, T. K. (2014). Bioelectrical impedance methods for noninvasive health monitoring: a review. *Journal of Medical Engineering, 2014*, 381251.

Brantlov, S., Andersen, T. B., Jødal, L., Rittig, S., & Lange, A. (2016). Bioimpedance spectroscopy in healthy children. *Journal of Clinical Engineering, 41*(1), 33–39.

Canali, C., Heiskanen, A., Muhammad, H. B., Hoym, P., Pettersen, F. J., Hemmingsen, M., Wolff, A., Dufva, M., Martinsen, O. G., & Emnéus, J. (2015). Bioimpedance monitoring of 3D cell culturing—Complementary electrode configurations for enhanced spatial sensitivity. *Biosensors and Bioelectronics, 63*, 72–79.

Caon, M. (2004). Voxel-based computational models of real human anatomy: a review. *Radiation and Environmental Biophysics, 42*(4), 229–235.

Cybulski, G. (2011). *Ambulatory impedance cardiography*. Berlin-Heidelberg: Springer.

Danilov, A. A., Kopytov, G. V., & Vassilevski, Y. V. (2017). Online simulator for bioimpedance measurements. Accessed November 10, 2017. http://dodo.inm.ras.ru/bia/

Danilov, A. A., Kramarenko, V. K., Nikolaev, D. V., & Yurova, A. S. (2013). Personalized model adaptation for bioimpedance measurements optimization. *Russian Journal of Numerical Analysis and Mathematical Modelling, 28*(5), 459–470.

Danilov, A. A., Nikolaev, D. V., Rudnev, S. G., Salamatova, V. Y., & Vassilevski, Y. V. (2012). Modelling of bioimpedance measurements: unstructured mesh application to real human anatomy. *Russian Journal of Numerical Analysis and Mathematical Modelling, 27*(5), 431–440.

de Sitter, A., Verdaasdonk, R. M., & Faes, T. J. C. (2016). Do mathematical model studies settle the controversy on the origin of cardiac synchronous trans-thoracic electrical impedance variations? A systematic review. *Physiological Measurement, 37*(9), R88–R108.

Dowrick, T., Blochet, C., & Holder, D. (2016). In vivo bioimpedance measurement of healthy and ischaemic rat brain: implications for stroke imaging using electrical impedance tomography. *Physiological Measurement, 36*(6), 1273–1282.

Gabriel, S., Lau, R. W., & Gabriel, C. (1996a). The dielectric properties of biological tissues: II. Measurements in the frequency range 10 Hz to 20 GHz. *Physics in Medicine and Biology, 41*(11), 2251–2269.

Gabriel, S., Lau, R. W., & Gabriel, C. (1996b). The dielectric properties of biological tissues: III. Parametric models for the dielectric spectrum of tissues. *Physics in Medicine and Biology, 41*(11), 2271–2293.

Geselowitz, D. B. (1971). An application of electrocardiographic lead theory to impedance plethysmography. *IEEE Transactions on Biomedical Engineering BME, 18*(1), 38–41.

Gosselin, M. C., Neufeld, E., Moder, H., Huber, E., Farcito, S., Gerber, L., Jedensjö, M., Hilber, I., Gennaro, F. D., Lloyd, B., Cherubini, E., Szczerba, D., Kainz, W., & Kuster, N. (2014). Development of a new generation of high-resolution anatomical models for medical device evaluation: the Virtual Population 3.0. *Physics in Medicine and Biology, 59*(18), 5287–5304.

Grimnes, S., & Martinsen, O. (2014). *Bioimpedance and bioelectricity basics* (3rd ed.) London: Academic.

Höhne, K. H., Pflesser, B., Pommert, A., Riemer, M., Schubert, R., Schiemann, T., Tiede, U., & Schumacher, U. (2000). A realistic model of the inner organs from the visible human data. In *Medical Image Computing and Computer-Assisted Intervention – MICCAI 2000* (pp. 776–785). Berlin: Springer Nature.

Holder, D. S. (2005). *Electrical impedance tomography*. Bristol: IOP.

Jaffrin, M. Y., & Morel, H. (2008). Body fluid volumes measurements by impedance: a review of bioimpedance spectroscopy (BIS) and bioimpedance analysis (BIA) methods. *Medical Engineering & Physics, 30*, 1257–1269.

Jindal, G. D., Sawant, M. S., Jain, R. K., Sinha, V., Bhat, S. N., & Deshpande, A. K. (2016). Seventy-five years of use of impedance plethysmography in physiological data acquisition and medical diagnostics. *MGM Journal of Medical Sciences, 3*, 84–90.

Kaporin, I. E. (1998). High quality preconditioning of a general symmetric positive definite matrix based on its $u^t u + u^t r + r^t u$-decomposition. *Numerical Linear Algebra with Applications, 5*(6), 483–509.

Kauppinen, P. K., Hyttinen, J. A., & Malmivuo, J. A. (1998). Sensitivity distributions of impedance cardiography using band and spot electrodes analyzed by a three-dimensional computer model. *Annals of Biomedical Engineering, 26*(4), 694–702.

Lipnikov, K. N., & Vassilevski, Y. V. (2007). Advanced numerical instruments 3D. Accessed November 10, 2017. https://sourceforge.net/projects/ani3d/

Ness, T. V., Chintaluri, C., Potworowski, J., Leski, S., Glabska, H., Wojcik, D. L., & Einevoll, G. T. (2015). Modelling and analysis of electrical potentials recorded in microelectrode arrays (MEA). *Neuroinformatics, 13*(4), 403–426.

Orschulik, J., Petkau, R., Wartzek, T., Hochhausen, N., Czaplik, M., Leonhardt, S., & Teichmann, D. (2016). Improved electrode positions for local impedance measurements in the lung—a simulation study. *Physiological Measurement, 37*(12), 2111–2129.

Patterson, R. P. (2010). Impedance cardiography: what is the source of the signal? *Journal of Physics: Conference Series, 224*, 012118.

Pettersen, F. J., & Høgetveit, J. O. (2011), From 3D tissue data to impedance using Simpleware ScanFE+IP and COMSOL Multiphysics—a tutorial. *Journal of Electrical Bioimpedance, 2*, 13–32.

Rineau, L., & Yvinec, M. (2007). A generic software design for Delaunay refinement meshing. *Computational Geometry, 38*(1–2), 100–110.

Saltarelli, A. J., Roseth, C. J., & Saltarelli, W. A. (2014). Human cadavers vs multimedia simulation: a study of student learning in anatomy. *Anatomical Sciences Education, 7*(5), 331–339.

Serra, J. (1984). *Image analysis and mathematical morphology*. London: Academic.

Ulbrich, M., Marleaux, B., Mühlsteff, J., Schoth, F., Koos, R., Teichmann, D., & Leonhardt, S. (2013). High and temporal resolution 4D FEM simulation of the thoracic bioimpedance using MRI scans. *Journal of Physics: Conference Series, 434*, 012074.

Vassilevski, Y. V. (2010). Mathematical technologies for electroimpedance diagnostics and monitoring of cardiovascular and respiratory diseases, Report. Accessed November 10, 2017 (in Russian). http://dodo.inm.ras.ru/research/_media/fcp/14.740.11.0844-report-1.pdf

Vassilevski, Y. V., Danilov, A. A., Nikolaev, D. V., Rudnev, S. G., Salamatova, V. Y., & Smirnov, A. V. (2012). Finite-element analysis of bioimpedance measurements. *Zhurnal Vychislitelnoi Matematiki i Matematicheskoi Fiziki, 52*(4), 733–745 (in Russian).

Xu, X. G. (2014). An exponential growth of computational phantom research in radiation protection, imaging, and radiotherapy: a review of the fifty-year history. *Physics in Medicine and Biology, 59*(18), R233–R302.

Yushkevich, P. A., Piven, J., Hazlett, H. C., Smith, R. G., Ho, S., Gee, J. C., & Gerig, G. (2006). User-guided 3D active contour segmentation of anatomical structures: significantly improved efficiency and reliability. *NeuroImage, 31*(3), 1116–1128.